# Global Precipitation Measurement (GPM) Ground Validation (GV) Prototype in the Korean Peninsula

JI-HYE KIM

*National Institute of Meteorological Research, Korea Meteorological Administration, Jeju-do, and Department of Atmospheric Sciences, Yonsei University, Seoul, South Korea*

MI-LIM OU

*National Institute of Meteorological Research, Korea Meteorological Administration, Jeju-do, South Korea*

JUN-DONG PARK

*National Meteorological Satellite Center, Korea Meteorological Administration, Jincheon, South Korea, and Earth System Science Interdisciplinary Center, University of Maryland, College Park, College Park, Maryland*

KENNETH R. MORRIS AND MATHEW R. SCHWALLER

*NASA Goddard Space Flight Center, Greenbelt, Maryland*

DAVID B. WOLFF

*NASA Wallops Flight Facility, Wallops Island, Virginia*

(Manuscript received 3 September 2013, in final form 13 March 2014)

ABSTRACT

Since 2009, the Korea Meteorological Administration (KMA) has participated in ground validation (GV) projects through international partnerships within the framework of the Global Precipitation Measurement (GPM) Mission. The goal of this work is to assess the reliability of ground-based measurements in the Korean Peninsula as a means for validating precipitation products retrieved from satellite microwave sensors, with an emphasis on East Asian precipitation. KMA has a well-developed operational weather service infrastructure composed of meteorological radars, a dense rain gauge network, and automated weather stations. Measurements from these systems, including data from four ground-based radars (GRs), were combined with satellite data from the Tropical Rainfall Measuring Mission (TRMM) precipitation radar (PR) and used as a proxy for GPM GV over the Korean Peninsula. A time series of mean reflectivity differences (GR − PR) for stratiform-only and above-brightband-only data showed that the time-averaged difference fell between −2.0 and +1.0 dB$Z$ for the four GRs used in this study. Site-specific adjustments for these relative mean biases were applied to GR reflectivities, and detailed statistical comparisons of reflectivity and rain rate between PR and bias-adjusted GR were carried out. In rain-rate comparisons, surface rain from the TRMM Microwave Imager (TMI) and the rain gauges were added and the results varied according to rain type. Bias correction has had a positive effect on GR rain rate comparing with PR and gauge rain rates. This study confirmed advance preparation for GPM GV system was optimized on the Korean Peninsula using the official framework.

## 1. Introduction

The Tropical Rainfall Measuring Mission (TRMM) has monitored the precipitation systems in the tropics and subtropics with active and passive microwave sensors since November 1997. The TRMM satellite includes the precipitation radar (PR) operating at 13.8 GHz (Ku band) and the TRMM Microwave Imager (TMI), which has nine horizontally and vertically polarized channels ranging from 10.65 to 85.5 GHz (Kummerow et al. 1998). The Global Precipitation Measurement (GPM) Mission builds on TRMM with an international constellation of

*Corresponding author address:* Mi-Lim Ou, National Institute of Meteorological Research, Korea Meteorological Administration, 33, Seohobuk-ro, Seogwipo-si, Jeju-do 697-845, South Korea.
E-mail: milim@korea.kr

DOI: 10.1175/JTECH-D-13-00193.1

© 2014 American Meteorological Society

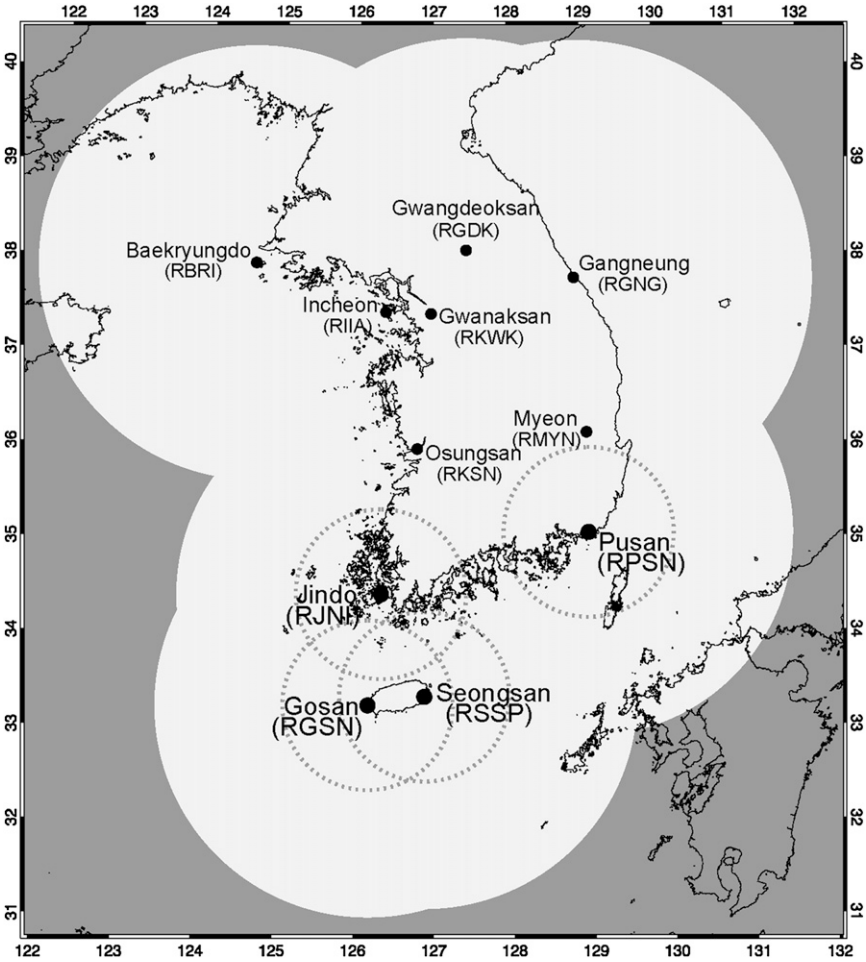


FIG. 1. The national radar network coverage map of KMA in the Korean Peninsula: KMA operational radar sites (small black dots) and coverage (white area). The four radar sites in the target domain of this study are marked with larger black dots.

research and operational satellites (Hou et al. 2008). The design of the GPM core satellite is similar to TRMM but with an active dual-frequency precipitation radar (DPR) and a passive GPM Microwave Imager (GMI). The GMI has 13 vertically and horizontally polarized channels that operate in the range of 10.65–183 GHz; the DPR includes a Ku-band (13.60 GHz) radar and a Ka-band (35.5 GHZ) radar (Hou et al. 2008). The addition of the higher-frequency channels on the GMI and DPR extends the capability of these instruments to observe light rainfall and snowfall, which will make up a significant fraction of the precipitation observed by the GPM core satellite in the higher latitudes of its 65° inclined orbit.

GPM satellite measurements will be made in concert with ground validation (GV) measurements collected from a variety of international sources. GV data sources will include long-term observations from national meteorological networks as well as measurements made as part of relatively short-term field campaigns. The overall goal of the GV operation is to contribute to GPM precipitation algorithm development and to verify precipitation retrievals. An additional goal of GPM GV is to support the integration of precipitation retrievals into hydrological applications.

The Korea Meteorological Administration (KMA) maintains well-established ground radars (GRs), and a dense rain gauge network and automated weather systems (AWSs) that will contribute to GPM GV. KMA operates 11 radar sites, including eight S-band (2.0–4.0 GHz) and three C-band (4.0–8.0 GHz) radars. The geographical coverage map of these radar sites is shown in Fig. 1. KMA also operates a network of 698 AWS stations with a spatial resolution of about 13 km, and each station reports precipitation measurements on 1-min intervals via an automated quality control system. Moreover, KMA has two intensive observation

TABLE 1. Characteristics of the four S-band radars.

| Site name | Site ID | Lat (°N) | Lon (°E) | Beamwidth (°) | Alt (m) | Range (km) |
|---|---|---|---|---|---|---|
| Jindo | RJNI | 34.473 | 126.324 | 0.89 | 500 | 240 |
| Pusan | RPSN | 35.119 | 128.999 | 0.97 | 549 | 240 |
| Gosan | RGSN | 33.294 | 126.163 | 1.00 | 103 | 250 |
| Seongsan | RSSP | 33.387 | 126.880 | 1.00 | 72 | 250 |

sites at Boseong, located at 34.763°N, 127.212°E, and at Daegwallyeong, located at 37.677°N, 128.718°E. Each intensive observation site includes a micro rain radar, an optical rain gauge, a synoptic weather observation, a microwave radiometer, and an optical disdrometer. Currently, there are also 93 conventional surface measurement sites, nine upper-air sites, 13 wind profilers, 21 lightning observation sites, 264 snow depth measurement sites (including 73 automated stations), three lidar stations and eight moored buoys, and 23 radar sites, including two Weather Surveillance Radar-1988 Doppler (WSR-88D) sites, nine Republic of Korea Air Force stations, and one research station with 11 KMA radars.

As part of the international GPM GV effort, the study described below was performed to compare data collected from a subset of KMA's national network of S-band radars and AWS rain gauges to satellite data collected by TRMM. Because of similarities in the TRMM and GPM instrumentation, this work is considered to be a prototype for the direct statistical validation that will be performed in the GPM era. Previous studies have compared TRMM PR reflectivities and rain rates with ground observation and demonstrated the utility of GRs to test the detection accuracy of PR and the performance of the PR attenuation correction algorithm (Bolen and Chandrasekar 2000; Schumacher and Houze 2000; Liao et al. 2001; Liao and Meneghini 2009a,b; Wang and Wolff 2009). Furthermore, rain gauges have been used for validation of precipitation retrievals from the TRMM TMI, other spaceborne microwave instruments, and precipitation products derived from these instruments (Simpson et al. 1988; Kummerow et al. 2001; Sohn et al. 2010). In this regard, the KMA ground validation data are specifically intended to improve the performance of GPM precipitation retrievals in and around East Asia.

Section 1 of this paper describes the basic concept of GPM GV in the Korean Peninsula and provides background information of KMA datasets. Section 2 provides details on the satellite, ground radar, and rain gauge data sources and data processing; GR and rain gauge rain-rate computation; and the PR–GR reflectivity and PR–GR–TMI–gauge rain-rate resampling algorithms. Section 3 discusses PR–GR reflectivity comparisons and rain-rate comparisons for PR, TMI, GR, and rain-gauge datasets that are scaled to the TMI field of view. Section 4 summarizes the statistical results and presents an outline for future work.

## 2. Data sources

This study uses TRMM version 6 PR 2A-25 radar reflectivity data and TMI 2A-12 rain-rate data collected during rain events from August 2006 to August 2010 when the satellite passed over four selected S-band ground radars (Table 1) within the KMA national network. Rain gauge data used in rain-rate comparisons are derived from 1-min-resolution data acquired from AWS stations surrounding the ground radars. A description of each dataset and the methods used to spatially and temporally match them for the purpose of intercomparison is given in the following sections. The use of version 6 TRMM products in this study rather than the current version 7 products allows us to make comparisons to previously published results. KMA had analyzed comparisons of PR and GR reflectivities and rain rates using versions 6 and 7 data in the same period applying the same matchup method with this paper. As a result, a few were noticeably different between the two versions in reflectivity distributions. In terms of rain rate, a comparison of PR version 7 with gauge and GR showed somewhat better results than version 6, which removed overestimations of PR. Zagrodnik and Jiang (2013) have shown the statistical analysis for TRMM PR and TMI in versions 6 and 7 compared to the stage-IV product over three surface types (land, ocean, and coast) around the southeastern United States. Through these results, we confirmed that the rain products have improved as the version was altered in the algorithm, but there were no severe differences between the two versions that overturn the validation results in this study.

### *a. TRMM PR reflectivity data*

TRMM PR measures returned radar signals from hydrometeors and the earth's surface and provides three-dimensional information on precipitation systems over the tropics and subtropics (Kozu et al. 2001). The precipitation radar makes observations between 1 and 3 times per day over any given location within its sampling

domain, depending on the latitude of the orbit (Negri et al. 2002).

Of the PR output data products, two kinds of radar reflectivity factors are available—the measured raw-calibrated radar reflectivity factor (1C-21) and the attenuation-corrected radar reflectivity (2A-25)—each at 5-km horizontal and 250-m vertical resolution. In the 1C-21 raw reflectivity, the effects of attenuation by cloud liquid water and water vapor are inherent in the return signals. For the 2A-25 attenuation-corrected reflectivities, path attenuation correction methods, including a hybrid of a Hitschfeld–Bordan (Hitschfeld and Bordan 1954) and a surface reference technique (Meneghini et al. 2000), are applied to the raw reflectivity. Several studies have evaluated the stability of the TRMM PR attenuation correction algorithm through comparisons of GR unattenuated radar reflectivities and the PR attenuation-corrected reflectivities measured near the surface (Liao and Meneghini 2009a; Wang and Wolff 2009). Quality control, beamfilling corrections, and clutter rejection near the surface are performed in the process of generating the 2A-25 product, but such corrections are not applied to the 1C-21 data (Kozu and Iguchi 1999; Iguchi et al. 2000).

In this study, only the PR 2A-25 reflectivity is used for comparison with the GR reflectivity. Available reflectivity data are limited to the range from the lowest clutter-free region (normally 1−2 km above the surface) to an altitude of about 20 km, as the radar echoes below the clutter-free region are not included in the 2A-25 dataset. The height of cluttered versus uncluttered boundary increases from the nadir point toward the edge of the observation swath.

### b. *Ground-based radar reflectivity data*

The GR scans a three-dimensional volume over a target area by making sweeps from a fixed location. S-band radar is regarded as suitable for characterizing instantaneous near-surface precipitation in dense resolution and quasi-continuous mode, because the attenuation at S band is significantly less than at C band. For this study, four S-band radars located close to the coast that are within the TRMM PR coverage area were selected: Jindo (RJNI) and Pusan (RPSN) on the southern coast of the Korean Peninsula, and Gosan (RGSN) and Seongsan (RSSP) on Jeju Island. RGSN was included in the GPM Ground Validation System (GVS) Validation Network (VN) in 2009 (Schwaller and Morris 2011). Table 1 presents the locations and characteristics of the four GRs used in this study. Note that RJNI and RPSN operate at 2.9 and 2.7 GHz, while RGSN and RSSP operate at 2.75 GHz. Volume scans of quality-controlled reflectivity for each radar site are produced every 10 min.

### c. *PR and GR reflectivity data matchup*

A PR and GR matchup method described by Schwaller and Morris (2011) was used to merge regional satellite overpass data and coincident ground radar observations in the same coordinates. To support the temporal matching of the PR and GR data, the orbit numbers, dates, and times when TRMM passed over the 100-km radius centered on the GR were calculated using the National Aeronautics and Space Administration (NASA) TRMM Overflight Finder program (http://pps.gsfc.nasa.gov/TOFF/). PR scan data and GR volume scan data collected within ±5 min of one another were spatially matched using the GPM Validation Network software Ground and Space Radar Volume Matching Comparison Software (http://opensource.gsfc.nasa.gov/). The VN method matches PR and GR radar data by calculating averages of PR reflectivity and GR reflectivity at the geometric intersection of the PR rays with the individual GR elevation sweeps. The algorithm thus averages the minimum PR and GR sample volumes needed to create a ''matchup'' of spatially coincident PR and GR data types. The result of this technique is a set of vertical profiles along PR rays for a given rainfall event, with coincident PR and GR samples matched at specified heights throughout the profile defined by the GR beamwidth and elevation scan strategy (see Fig. 2). This method has been found to provide a more precise estimate of PR–GR bias when compared to methods that use uniform spatial grids for PR–GR comparisons (Morris and Schwaller 2011).

Coincident PR and GR data were used in this study only in the cases of ''significant precipitation events,'' defined as where 100 or more samples were identified as ''rain certain'' in the PR metadata for stratiform or convective rain falling within a 100-km radius of the ground radar.

TRMM PR has a minimum detectable signal of ~18 dB$Z$ (Kozu et al. 2001), whereas the KMA GRs can detect much lower reflectivities with higher sensitivity. An artificial detection threshold of 15 dB$Z$ was defined for the GR to limit the bias between the PR and GR for reflectivities near and below the PR detection threshold while allowing for a calibration offset of up to 3 dB$Z$ between the two systems. For the data analyzed in all the comparisons to follow, matched volumes are included only if >90% of all preaveraging radar range bin observations within the volume have a reflectivity of ≥18 dB$Z$ (for PR) and ≥15 dB$Z$ (for the GRs). The numbers of PR/GR coincident events meeting the rain-certain event criterion and having one or more volume-match samples that meet the 90% above-threshold criterion for dates from August 2006 to August 2010

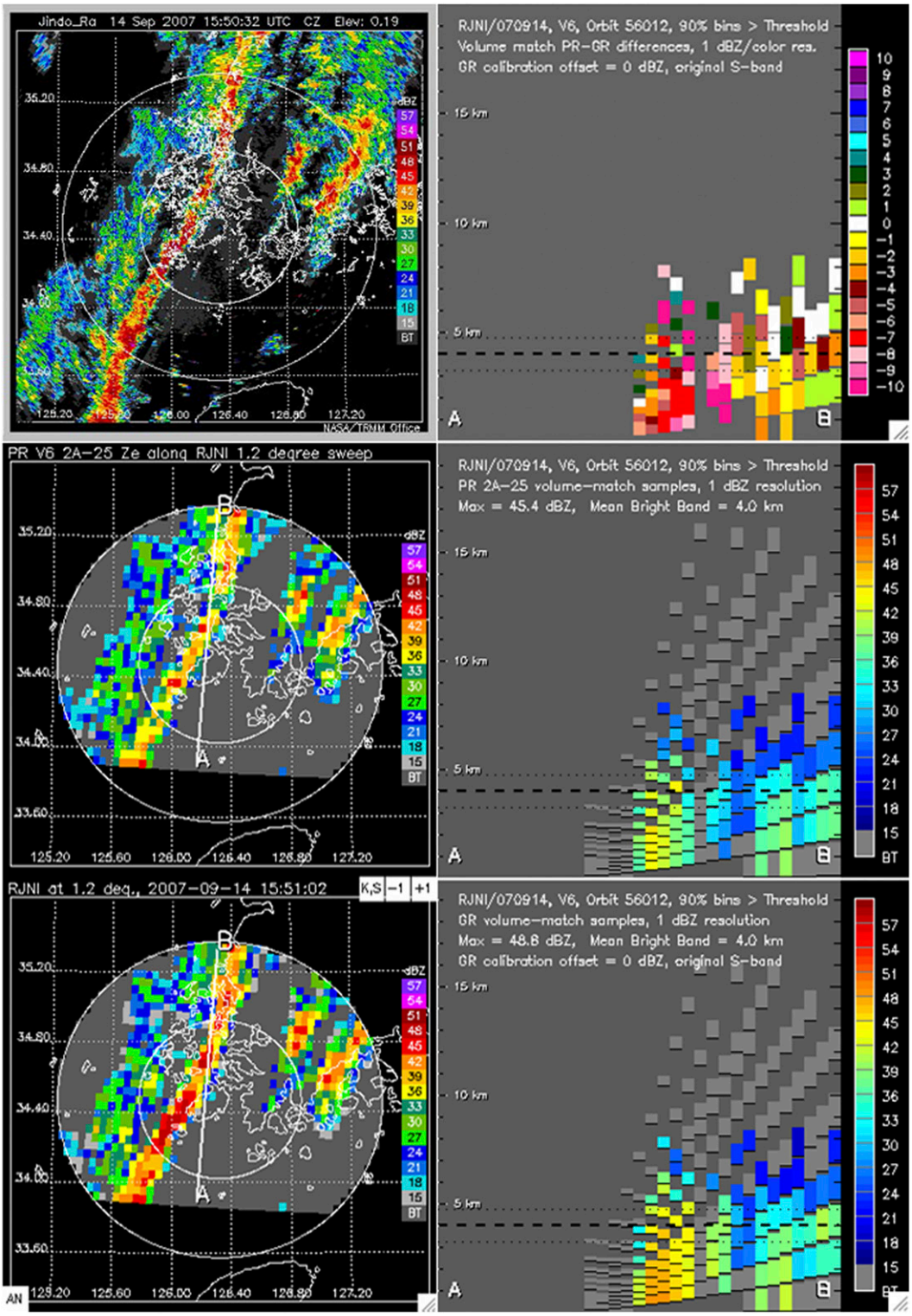


FIG. 2. The visualizations of the statistical analysis for one precipitation case (14 Sep 2007) at the RJNI site. (left top) The full-resolution GR plan position indicator (PPI) at 0.19° elevation from the original Universal Format (UF) file, and (left middle) the volume-matched PR and (left bottom) the GR data corresponding to the 1.2° elevation sweep of the GR. A vertical cross section of (right middle) PR and (right bottom) GR reflectivity and (right top) PR–GR reflectivity difference over all GR elevation sweep surfaces, from volume-matched data, for samples along the PR scan line labeled A–B in the PPIs. Samples not meeting the 90% above-threshold constraint (see text) are presented as gray boxes in the PR and GR cross sections (middle) and (bottom). The heavy dashed line on the cross sections indicates the mean bright band height (4.0 km) identified in the PR 2A-25 data for the case.

are 291 at RJNI, 215 at RPSN, 211 at RGSN, and 213 at RSSP.

### d. TRMM PR rain rate

TRMM PR rain rate was from the unmodified near-surface rain-rate variable in the 2A-25 product, and they have the same horizontal resolution and location as the volume-matched data, by definition.

### e. GR rain rate

GR rain rate, $R$ (mm h$^{-1}$), was calculated using the $Z = aR^b$ relationship. Values derived from an assumption of a Marshall–Palmer drop size distribution were used for stratiform and mixed-type rain: $a = 200$, $b = 1.6$. For convective rain the WSR-88D convective $Z$–$R$ relationship was used: $a = 300$, $b = 1.4$. The rain type for the GR was taken from the matching PR volumes, with adjustments as described in section 3a. The GR rain rate for each stratiform and convective sample was obtained by applying the respective $Z$–$R$ relationship to the PR-resolution, volume-matched GR reflectivity values computed on a 1.5-km AGL constant altitude plan position indicator (CAPPI) surface. The resulting GR rain-rate samples have a one-to-one relationship with the PR 2A-25 near-surface rain rate, but the $Z$–$R$ relationship applied to GR reflectivity in a large footprint identical to PR resolution could cause partial beamfilling errors. According to Durden et al. (1998), the simulated rain rate by the $Z$–$R$ relationship at PR resolution (~4 km) was overestimated about 3% relative to the beamfilling error, since attenuation is neglected in the rain retrieval. As the four S-band radars considered in this study are mostly not affected by attenuation, this result seems to be working in the calculation of the GR rain rate.

### f. TRMM TMI rain rate

The measurement swath of TMI is 760 km, which is 3 times as large as that of PR. For the 2A-12 standard product, radiometric microwave radiances detected on nine channels of the TMI sensor are converted into instantaneous hydrometeor profiles and surface rain using the Goddard profiling algorithm (GPROF). Hydrometeor profiles are gridded at a scale of 5-km horizontal resolution for 14 vertical levels, and the surface rain rate is assigned at approximately a 150 km$^2$ horizontal resolution in the TMI footprint (Kummerow et al. 1998; Olson et al. 2006). The 2A-12 version 6 rain algorithm, which is an operational version of GPROF, applies different methods for rain-rate retrieval over ocean, coast, and land, each with different physical assumptions of the surface microwave radiance (Kummerow et al. 2001). Over the oceans GPROF applies a physical algorithm based on the Bayesian theorem (Kummerow et al. 1996; Olson et al. 1999) that utilizes the radiometric signals from emission channels of lower frequencies. However, the increasing emissions become saturated at rain rates greater than about 20.0 mm h$^{-1}$ (Ha and North 1999). For pixels classified as over a land surface, the rain algorithm takes notice of radiative reduction by scattering from frozen hydrometeors above the freezing level in the 85.5-GHz channel, ignoring the lower frequencies because emission signals from liquid hydrometeors are covered by high background temperature over land surfaces. Spencer et al. (1989) suggested that there is an empirical relationship between the reduced amounts of brightness temperature (Tb) at 85.5 GHz and surface rain rate. GPROF currently applies a rain algorithm over land that is described in Ferraro (1997) and McCollum and Ferraro (2003). However, in coastal regions where the four GRs are located, there are large horizontal variations within a TMI footprint due to different radiometric contributions by the ocean and land. In this case, the rain rate for TMI footprints used in this study will have been determined from empirical relations suggested in McCollum and Ferraro (2005).

### g. Rain gauge rain rate

Rain gauge data are affected by systematic and sampling errors, including mechanical and electrical problems such as inadequate calibration, wind effects, evaporation from funnel surface, etc. (Humphrey et al. 1997; Nespor and Sevruk 1999; Habib et al. 2001; Wolff et al. 2005; Wang et al. 2008). However, rain gauges provide meaningful direct measurements for validation of GV radars and related satellite observations. Rain gauges installed in the Automated Weather Systems are equipped with a 0.5-mm tipping bucket, and they estimate the 1-day accumulated rain from samples taken at 1-min intervals. The instantaneous rain rate (mm h$^{-1}$) was estimated with 10-min intervals from the 1-min rain gauge tip data using the TRMM-gauge software package (GSP) algorithm (Wang et al. 2008). Rain gauge rain rates are affected by gauge sampling–related errors from the coarse time interval between two consecutive tips of the gauge bucket, and the errors vary with the type of rain event. For example, in light rain of less than 1.0–2.0 mm h$^{-1}$, where consecutive tips are separated by intervals of time much greater than 1 min, rain-rate observations from gauges are more likely to contain significant errors (Wang et al. 2008).

### h. Rain-rate matchup

PR and GR volume-matched rain-rate data from the spaceborne and ground-based radars were compared with rain-rate data from the TMI instrument, and with instantaneous rain gauge measurements as described

below. In this study, only those observations within a 100-km radius centered on the GR were included in the analysis. Coincident PR, GR, and rain gauge data were matched to corresponding TMI sample locations, defined as an area with a 7-km radius centered on the geographic location of the TMI footprint as given in the 2A-12 product. PR and GR rain-rate samples falling within each TMI footprint area were spatially averaged according to the method described by Wolff and Fisher (2008). Gauge rain rates for cases of multiple gauges located within a given TMI footprint were also spatially averaged. The temporal matching process is not included, because the gauge rain rate at the same time with all the matched up TRMM and GR data is available from GSP. The means of the PR, GR, and rain gauge rain rates were compared with TMI rain-rate data for cases where the rain rates for the gauge and radar sources were $\geq 0.0\,\mathrm{mm\,h^{-1}}$. The dominant rain type of each matched sample was classified by computing the fraction of PR-derived convective rain type (convF) within each area-averaged sample (Seo et al. 2007), where stratiform is $0.0 \leq \mathrm{convF} \leq 0.3$, mixed type is $0.3 < \mathrm{convF} \leq 0.7$, and convective is $0.7 < \mathrm{convF} \leq 1.0$.

## 3. Analysis and results

### a. Comparisons of the PR and GR reflectivities

In several reflectivity comparisons, mean values were calculated by linear average of dB$Z$ in each unit pixel in order to analyze distributions of arithmetic mean differences of PR and GR for 4 years. For the analysis of vertical profiles, PR and GR matchup volumes were each assigned into one of 19 vertical layers centered between 1.5 and 19.5 km above ground level, each with a spacing and depth of 1.5 km. The reflectivity samples placed at intervals of 1.5 km were averaged within each interval bin. Figure 3 displays the mean vertical profiles of the attenuation-corrected PR 2A-25 and GR reflectivities for the whole period of data. Rain pixels were distributed mainly within an altitude of 1.5–6 km, whereas above 10.5 km there were too few matching points to perform a statistically meaningful analysis. The layer-averaged reflectivities of PR and GR at RJNI showed quite similar values for levels above the bright band (freezing level), with mean differences of <1 dB$Z$ within and below the bright band (BB). The mean profile of GR at RPSN was nearly the same as the corresponding mean PR sample from 1.5- to 6-km altitude, but there were significant differences above the BB, with the GR generally running about 2 dB$Z$ lower than the TRMM PR. At the RGSN and RSSP sites, the PR reflectivities were higher than those of the GR by about 2–3 dB$Z$ for all levels. The profiles generally maintained a high reflectivity value up to an altitude of 4.5 km near the mean BB, which is the altitude at which the temperature profile crosses 0°C. The melting ice particles near the BB generate a large backscattered signal, as if they were large water drops. Hence, the BB is distinguished by the peak reflectivity in the vertical profile of the radar measurements, which showed up as an inflection at 4.5 km in the mean profiles. The layer-averaged reflectivity rapidly decreased with altitude and increased again at altitudes above 7.5 km owing to the changeover from predominantly stratiform rain type samples in lower layers to a deep convective regime at high levels.

Additional analyses were conducted to evaluate the systemic differences between TRMM PR and GR reflectivity according to categories related to the BB height (BBH) and the rain type. The categorization of matchup volumes by proximity to the BB (above, within, and below) and by rain type (stratiform and convective) is as follows. If the base (top) of the matchup sample is 750 m or higher (750 m or lower) than the mean BBH, then this is classified as above (below) the BBH. Points between the two layers are classified as being within the BB. The generous depth of the BB layer definition is to account for uncertainties in the mean PR-measured BBH and the GR beam heights, so that brightband-affected samples are safely excluded from the above- and below-BB categories. The BB-classified data are further separated into cases of stratiform and convective rain, based on the rain type assignments in the PR 2A-25 products. Results comparing the classified PR and GR reflectivities for each of the GRs are illustrated in Fig. 4. Except for RJNI, all of the mean values and modes of the GR–PR reflectivity differences in all categories were negative; that is, the RPSN, RGSN, and RSSP GRs exhibited lower reflectivities than the PR. Figure 4 also shows that RJNI reflectivities run higher on average than the TRMM PR above the BB, a result similar to that illustrated in Fig. 3. RJNI also measured higher reflectivities than PR in the stratiform, within-BB case, but it trends lower than PR in the below-BB case, a result similar to that seen in the other three GV radars. Note that in this study over 90% of the total rainy matchup samples were categorized as stratiform rain and therefore the results illustrated in Fig. 4 for the "total" and "stratiform" cases were very similar. The standard deviations of the PR and GR differences for the stratiform rain above BB were the smallest compared to those for other BB ranges as well as the convective rain above BB. Also, Fig. 4 shows that there are no remarkable differences among the results separated by surface type.

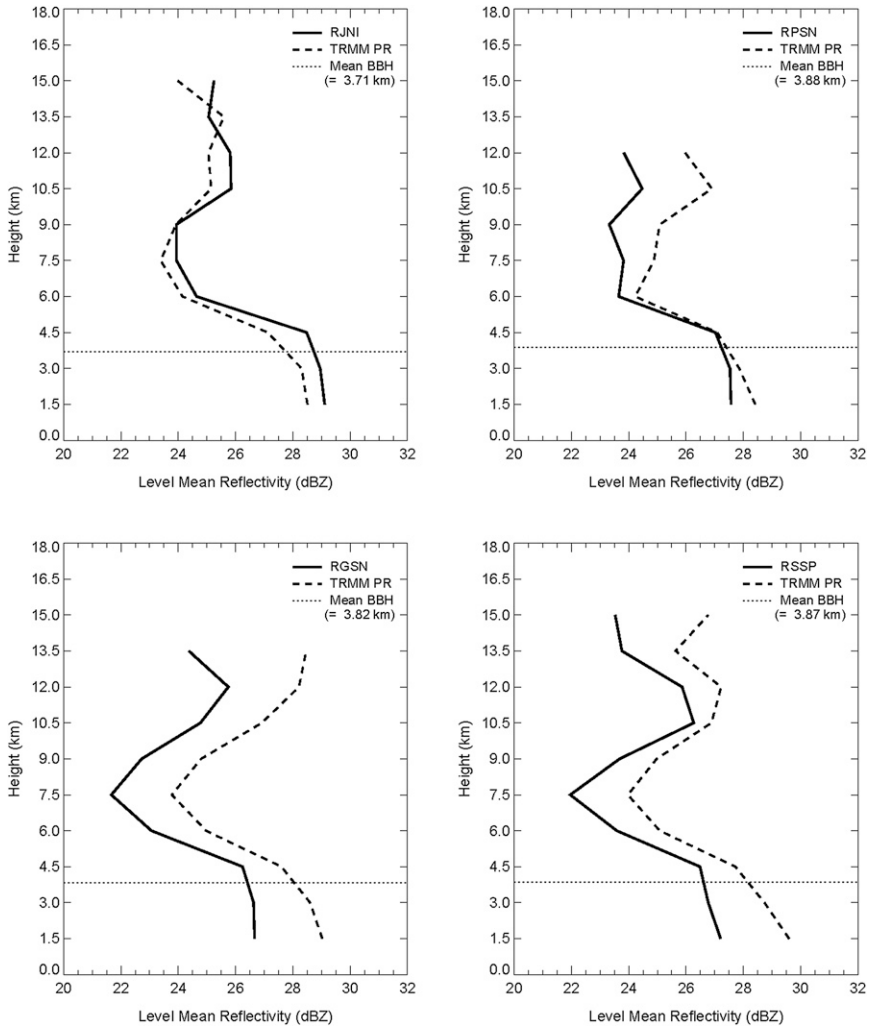


FIG. 3. Layer-averaged reflectivity distributions for the TRMM PR and (top left) unadjusted RJNI, (top right) RPSN, (bottom left) RGSN, and (bottom right) RSSP ground radars from August 2006 to August 2010. The horizontal dashed line indicates the mean BBH in samples for the period.

A time series of the differences between PR and GR reflectivities is shown in Fig. 5. The mean biases between the PR and GR reflectivities averaged for each rain case were arranged in chronological order for 4 years. Only the reflectivity pixels belonging to the stratiform rain type above the BB were included in these comparisons because the reflectivities in the convective rain below the BB may involve the following: 1) potential PR attenuation correction errors, 2) uncertainties associated with the large gradients of reflectivity in convective rain (Rosenfeld et al. 1992), and 3) random effects related to rain type changes (Wang and Wolff 2009). For each GR site, one or two rain events were eliminated as outliers because their mean differences exceeded the range of $\pm 10$ dB$Z$. The mean biases averaged for each case in the period illustrated in Fig. 5 were 0.868, $-0.270$, $-1.875$, and $-1.696$ dB$Z$ at RJNI, RPSN, RGSN, and RSSP, respectively. The averaged discrepancy of RJNI was biased toward the positive in the GR–PR reflectivity, which was opposite of the results for the other GRs. Two radars within a homogenous precipitation area and located close to each other (RSGN and RSSP) showed quite similar performance. The trends in the annual biases suggest that the differences in the reflectivities at RJNI, RGSN, and RSSP oscillate around their period averages, while those at RPSN exhibit rather wide fluctuations in the period from 2006 to 2009 but have trended closer to the average since 2009. These results are within the range of performance observed by other investigators [e.g., National Center for Atmospheric

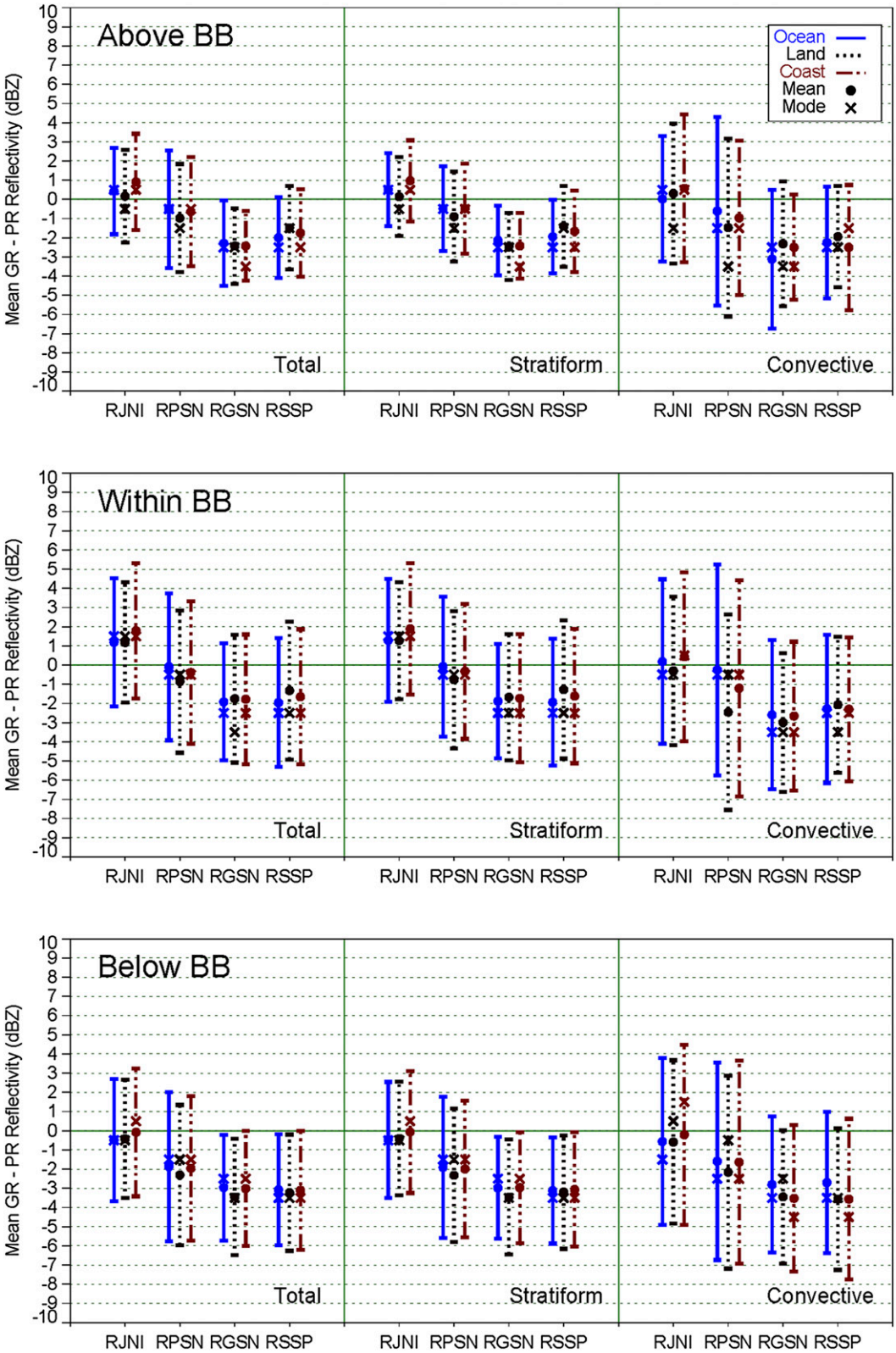


FIG. 4. Mean (dot), mode (X), and error bar (mean plus/minus standard deviation) of differences of PR and unadjusted GR reflectivities at RJNI, RPSN, RGSN, and RSSP for the entire period from August 2006 to August 2010. The results are divided into BBH criteria (above, within, and below), rain type (total, stratiform, convective), and surface type (ocean, land, and coast).

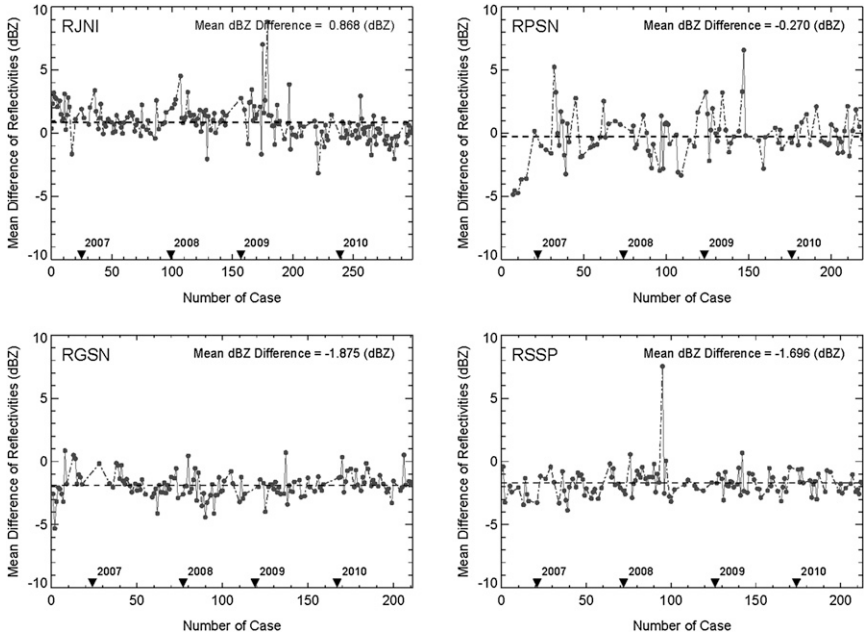


FIG. 5. Time series of mean reflectivity differences (GR − PR) for stratiform, above-BBH-only data collected by TRMM PR and (top left) unadjusted ground radars RJNI, (top right) RPSN, (bottom left) RGSN, and (bottom right) RSSP from August 2006 to August 2010. The horizontal dashed line indicates the average of the mean reflectivity differences in each event over the entire time period.

Research (NCAR) S-band polarization radar (S-POL); Melbourne, Florida, WSR-88D (KMLB); Large-Scale Biosphere-Atmosphere Experiment (LBA)–S-POL during the TRMM Field Campaign; Colorado State University–University of Chicago–Illinois State Water Survey (CSU–CHILL) radar during the Severe Thunderstorm Electrification and Precipitation Study (STEPS) campaign], where similar methods found the average stratiform unattenuated PR reflectivity to be 1.0–1.5 dB$Z$ higher than matched GR reflectivity (Bolen and Chandrasekar 2000; Anagnostou et al. 2001; Bolen and Chandrasekar 2003; Liao and Meneghini 2009b). The differences in reflectivities of PR and GR have been explained with significant characteristics of each sensor relative to the non-Rayleigh scattering effect at the PR frequency, polarization effect, and signal attenuation (Liao et al. 2001), and even if both radars are well calibrated, the sensitivity change of the two instruments with increasing distance from the GR site or the PR nadir line can also influence the difference in measurements (Gabella et al. 2006).

Following the method used by Liao and Meneghini (2009b), GR reflectivity was adjusted for bias by subtracting the radar's relative bias to PR in stratiform rain above BB, noted in Table 2. The biases at each GR site were calculated as the mean GR–PR reflectivity difference for every above-BB sample, classified by rain types. This bias-adjusted ground radar reflectivity was used in all subsequent analyses described below.

The scatterplots and the probability density function (PDF) analysis of the instantaneous reflectivities of the PR and GR are shown in Figs. 6–9. No averaging or smoothing was applied to matchup volume reflectivity values used in the scatterplots and PDF plots. The results are divided into six categories: a combination of three BB levels (above, within, and below) and two rain types (stratiform and convective). The solid line in the scatterplots is a regression line fitted to the PR and GR samples, and the diagonal dotted line represents the 1:1 line (PR = GR). Colors in the plots were assigned to boxes representing 1-dB$Z$ reflectivity intervals along the $x$ and $y$ axes. Colors were assigned to each box based on

TABLE 2. Mean biases of (GR − PR) reflectivities above BB for two rain types at the four S-band radars.

| Site ID | Rain type | Mean bias |
|---|---|---|
| RJNI | Stratiform | 0.648 |
| | Convective | 0.254 |
| RPSN | Stratiform | −0.565 |
| | Convective | −0.792 |
| RGSN | Stratiform | −2.173 |
| | Convective | −3.058 |
| RSSP | Stratiform | −1.887 |
| | Convective | −2.245 |

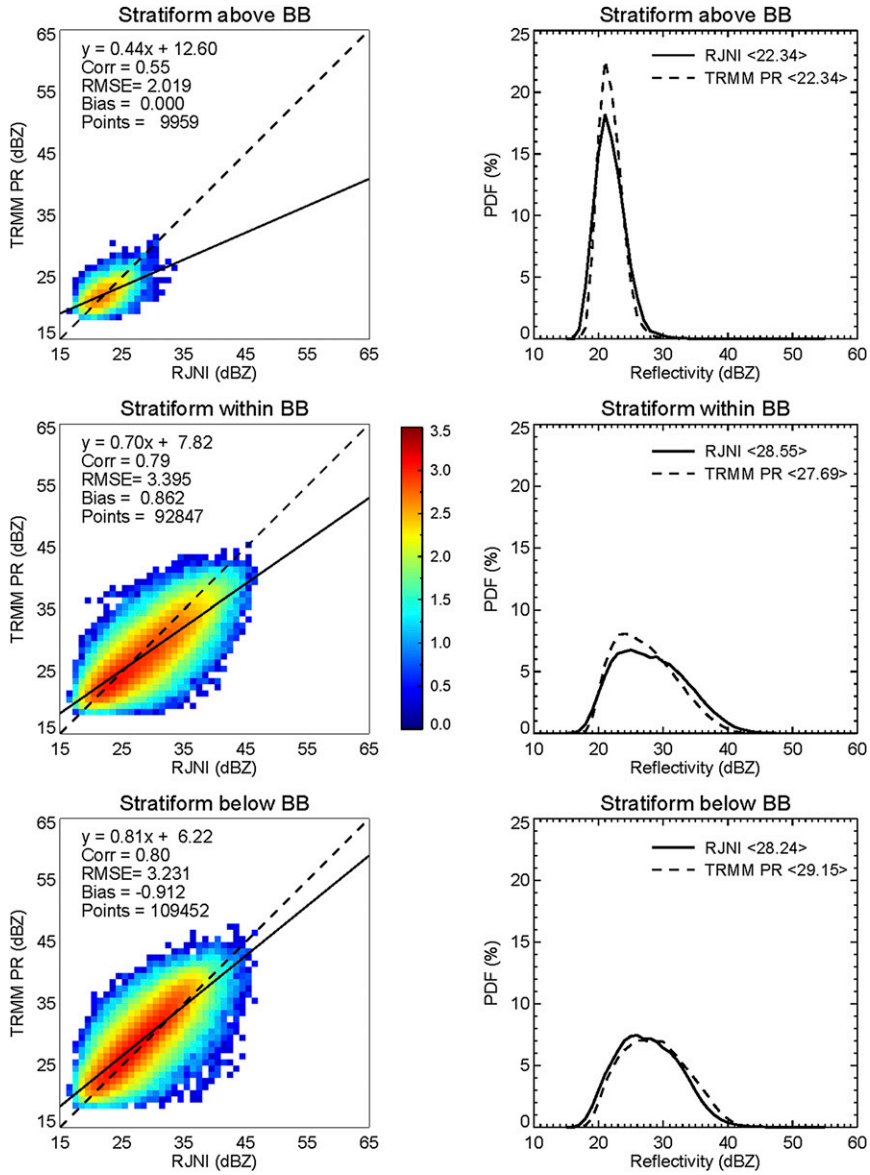


FIG. 6. (left) Scatterplots and (right) PDFs of reflectivity from the TRMM PR and bias-adjusted GR at RJNI from August 2006 to August 2010 for the BBH criteria: (top) above, (middle) within, and (bottom) below for stratiform rain. Color scale represents the $\log_{10}$ of the number of samples falling within each of the boxed intervals. The dashed line is the 1:1 line, and the solid line is the fitted regression line in the scatterplots. In the PDFs, PR is plotted as dashed lines and GR as solid lines. Bias was calculated by GR–PR.

the $\log_{10}$ of the number of samples falling within each of the boxed intervals. Note that in all cases, the number of stratiform samples was larger than the convective, and most of the reflectivities <25 dB$Z$ are from stratiform rain events.

Figures 6 and 7 compare reflectivity measured at RJNI versus the corresponding PR reflectivity for stratiform and convective rain. The maximum sample density within and below the BB fell within the 25–35-dB$Z$ range and generally trends along the 1:1 line. In the above-BB case, the PR reflectivity in the 25–35-dB$Z$ range tended to run lower than the GR, although there were a relatively small number of samples in this range. The characteristics of the PR and GR scatterplots were also seen in the peaks and shapes of the PDFs. The shapes of PR and GR reflectivity PDFs were similar, with the mean of PR reflectivities within BB smaller than GR by about 0.86 dB$Z$, while the mean values of PR and GR above

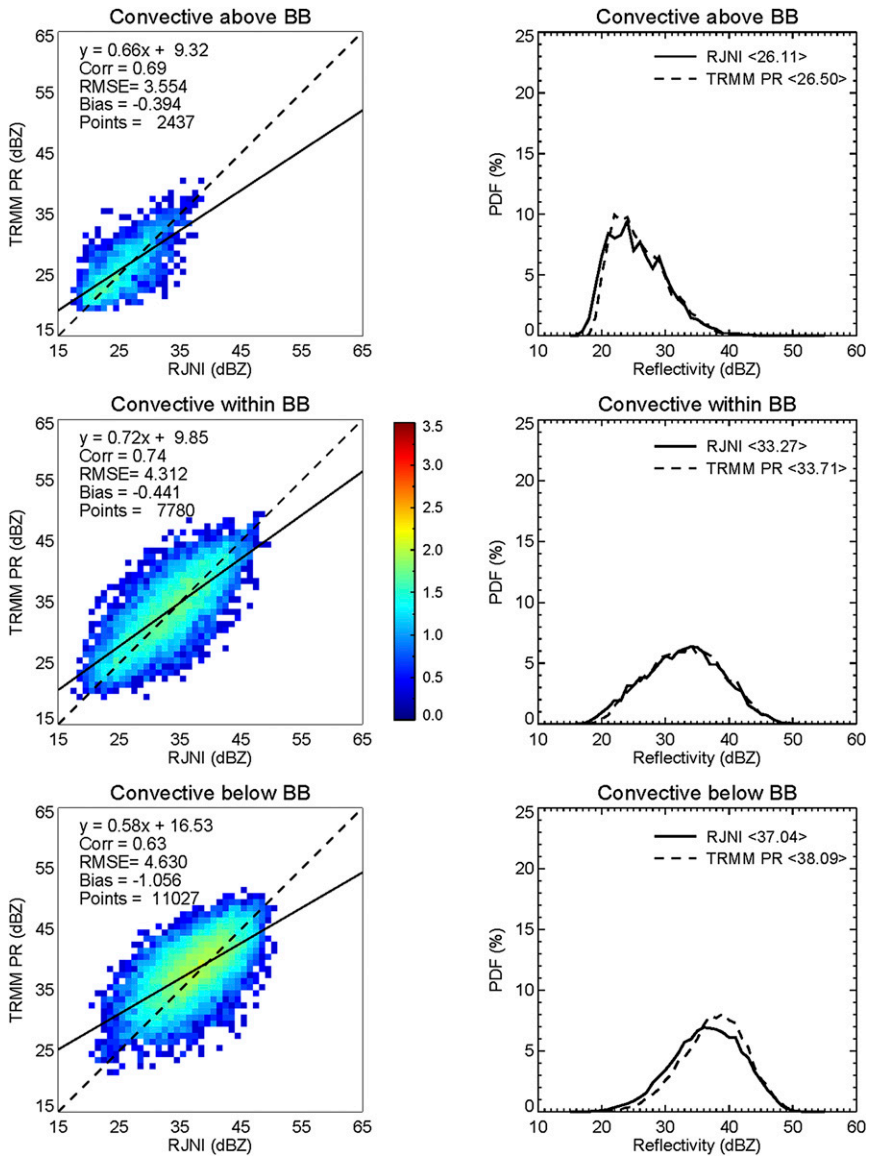


FIG. 7. As in Fig. 6, but for convective rain.

BB had become identical by bias adjusting the GR. Unlike this result, the mean difference of PR and GR increased in the below-BB case from −0.26 to about −0.91 dB$Z$ by the bias adjustment. Significant concentrations of PR and GR samples seen in the 20–22-dB$Z$ regions for the stratiform, above-BB category, especially in PR observations, can be related to tiny ice crystals about the same size as that in stratiform rain. The low density of hydrometeors in stratiform rain above the BB restricts their growth into large ice crystals. The PDFs for stratiform rain had a smooth shape, whereas the PDFs of PR and GR for the convective rain, where strong attenuations in reflectivities and fewer samples are evident, seem to have multiple peaks. In the convective rain case of Fig. 7, the peaks of the reflectivity distributions were found where sample values are ≥30 dB$Z$, except in the above-BB case. The number of samples in the convective case was fewer than in stratiform rain, and the root-mean-square errors (RMSEs) were larger. Correlations within BB were 0.74, but PDFs of PR and GR reflectivities nearly agreed with each other. The mean differences were also less than 1.0 dB$Z$.

Results illustrated in Figs. 8 and 9 (RSSP on Jeju Island) are similar to those in Figs. 6 and 7 (RJNI on the southwest coast of the mainland). There were more rain pixels in the range of below BB than other ranges at RJNI, whereas the largest percentage of pixels was included in the within-BB range at RSSP. As we can see in

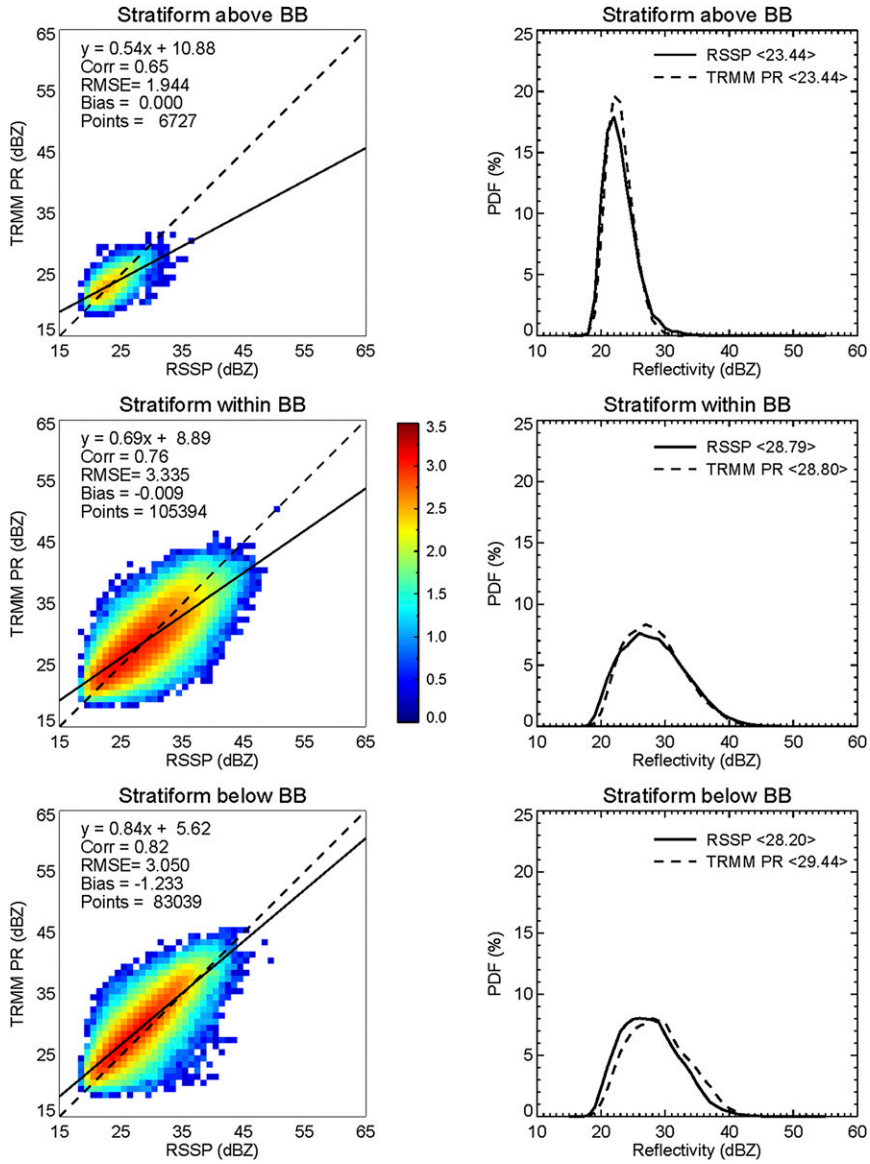


FIG. 8. As in Fig. 6, but for RSSP GR site.

Figs. 3–5, the distribution of the PR reflectivity was shifted to higher values compared to the original RSSP GR by about 2–3 dB$Z$ on average. After the bias adjustment for GR, points of GR and PR reflectivity corresponding to maxima frequencies of PDF were consistently above the 1:1 line on the scatterplot. This was also observed in the PDFs of Figs. 8 and 9.

### b. *Rain-rate comparisons*

To understand the statistical significance of distributions of remotely estimated rain rates from PR, TMI, and GR, these rates were compared with the gauge rain rate in the form of scatterplots and histograms. As in the reflectivity comparisons in the preceding section, the GR rain rate was obtained from reflectivities adjusted to remove the stratiform, above-BB mean GR bias against PR, shown in Table 2. The statistical values were calculated from the total rain type (stratiform, mixed type, and convective). At RJNI, GR rain rates were generally underestimated more than the rain gauge in the interval of 10.0–20.0 mm h$^{-1}$ for stratiform rain, while the mixed and convective rain rates showed overestimations with wide variations. PR rain rates were only slightly more closely correlated with the gauge rain rates (correlation = 0.40) than GR (correlation = 0.32), because PR tends to overestimate rain rates for mixed rain and convective rain types in

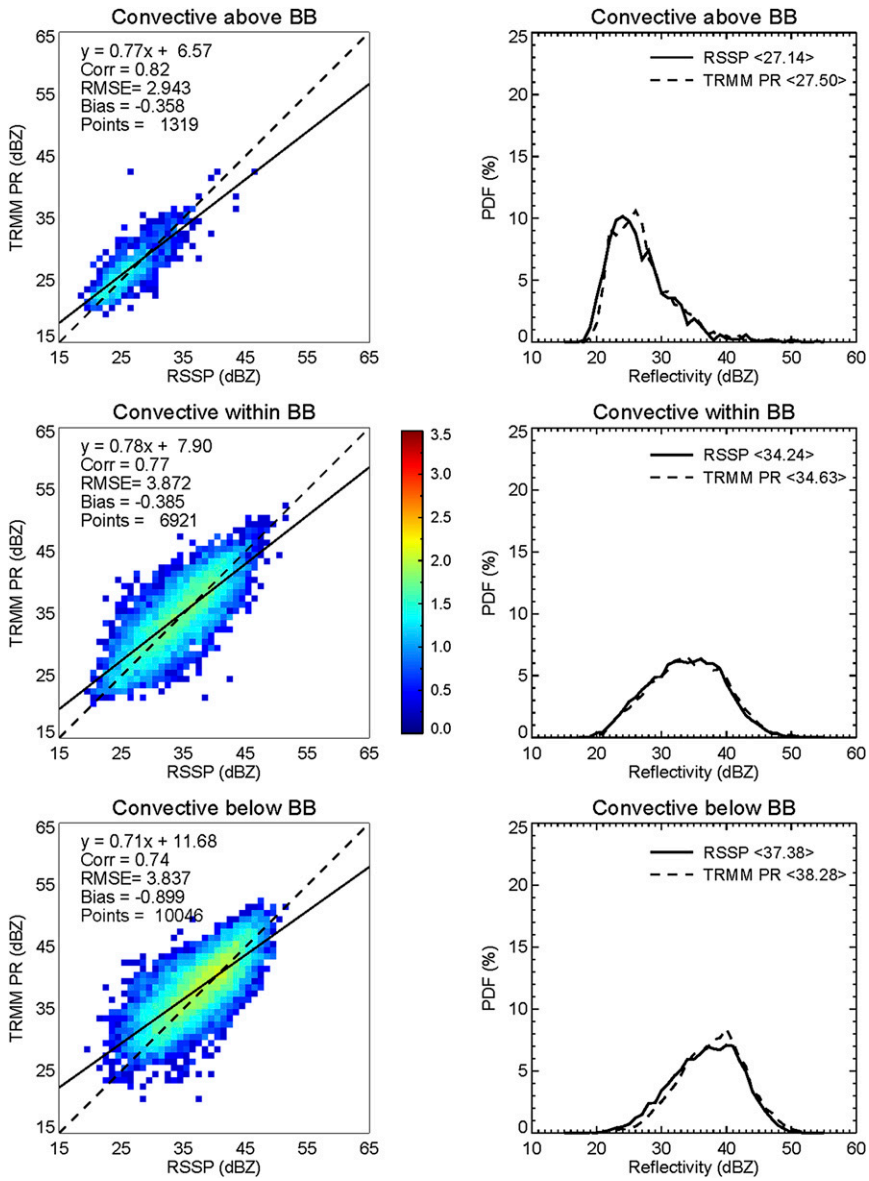


FIG. 9. As in Fig. 8, but for convective rain.

the 0.0–10.0 mm h$^{-1}$ range as much as GR underestimated stratiform rain rates in the 10.0–20.0 mm h$^{-1}$ range. As a result, the RMSE and bias of PR were slightly larger than those of GR. TMI rain rates were significantly underestimated when compared with the gauge rain rates, with outliers for gauge rates above 20.0 mm h$^{-1}$ as well as a considerable number of TMI values of 0.0 mm h$^{-1}$ paired with nonzero gauge values. The correlation with gauge rain (correlation = 0.27) was poorer than for PR and GR, but the RMSE was lower, and the bias was less than that of the PR. RJNI had the largest number of rain pixels among the four GV sites, and the more intense rain rates occurred more frequently. PR samples at RSSP had a similar pattern to those at RJNI, and TMI and GR had fewer outliers over 10.0 and 20.0 mm h$^{-1}$ in convective rain. Correlations of PR and GR rain rates with gauges were greater than that of RJNI samples by about 0.02; however, the RMSEs and biases were larger. In the case of TMI, the correlation was lower than RJNI by as much as 0.1. The number of rain pixels for the near-ocean RSSP site is smaller than for RJNI because the rain gauges are sparse in the former's area. The numbers of gauges assigned for each target area of the GR sites are 70 at RJNI, 81 at RPSN, 28 at RGSN, and 32 at RSSP.

The histograms of each of the rain-rate data for stratiform rain at RJNI, as shown in Fig. 10, revealed

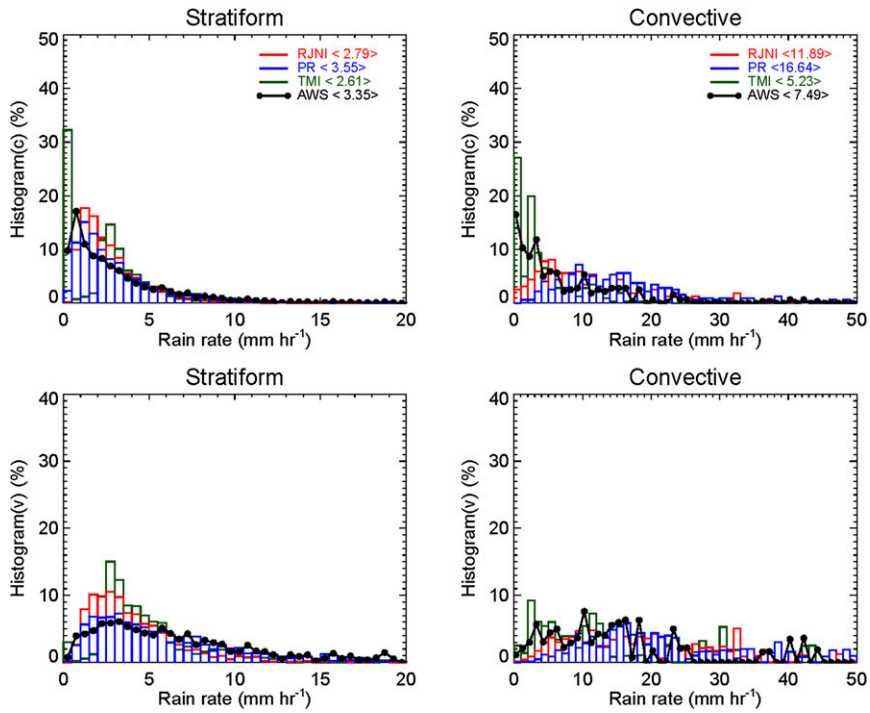


FIG. 10. Histograms of PR, TMI, GR, and rain gauge (AWS) rain rate at TMI footprint scale for August 2006 to August 2010 at RJNI. Shown are sample count histograms for (top left) stratiform rain, (bottom left) volumetric histograms for stratiform rain, (top right) sample count histograms for convective rain, and (bottom right) volumetric histograms for convective rain. Volumetric histogram is defined by frequency(c) multiplied by the rain-rate bin value of each interval.

significant differences among the measurement systems in the light rain category. The peak of the gauge rain rate was located in the 0.5–1.0 mm h$^{-1}$ bin for light stratiform rain in terms of number of pixel count [histograms(c)], which was the expected range considering the rain gauge minimum detectable rate of 0.5 mm h$^{-1}$. PR and GR showed similar distributions of rain rates with the rain gauge over the entire range, and their peaks and high-frequency bins were at higher rates than those of the gauge and TMI. In the same analysis, nonzero TMI-derived rain samples were concentrated in the 2.5–3.5 mm h$^{-1}$ with a large number of 0.0 mm h$^{-1}$ values in the 0.0–0.5 mm h$^{-1}$ bin. In the case of convective rain, peaks of TMI clustered in light rain below 3.0 mm h$^{-1}$ were in common with the stratiform result, while the GR and PR samples were concentrated in ranges of 4.0–6.0 mm h$^{-1}$ and near 10.0 and 15.0 mm h$^{-1}$, respectively.

The volumetric histograms [histogram(v)] obtained by multiplying histogram(c) by its bin value represented distributions spread more toward large rain-rate bins than that of histogram(c). This shows the quantitative distribution of rain rate measured at each sensor. In histogram(c) and histogram(v), PR rain had the closest pattern to the gauges in stratiform rain at RJNI. The pattern of GR rain rates also closely resembled those of PR and gauge, except for distinct peaks of GR at 1.0–2.5 mm h$^{-1}$. TMI rain rates in 2.5–3.5 mm h$^{-1}$ for stratiform rain accounted for 30% of the overall TMI rain-rate frequency.

The distributions of rain rates at RSSP as shown in Fig. 11 were similar to RJNI, with the distributions shifted slightly toward lower ranges than those of RJNI. The four kinds of rain-rate measurements for stratiform rain had, in general, a narrow distribution within the 0.0–5.0 mm h$^{-1}$ range, in contrast to a flatter distribution for convective rain spread over 0.0–30.0 mm h$^{-1}$. TMI rain rates were quite concentrated between 0.0 and 0.5 mm h$^{-1}$ for stratiform rain and between 0.0 and 1.0 mm h$^{-1}$ for convective rain, where these bins accounted for above 40% of the entire frequency range. The difference in the frequency of occurrence between TMI rain rates at RSSP and RJNI in these ranges was about 10%. The distribution of gauge rain for stratiform was analogous to that of RJNI, except that the rain rates of 0.5–1.0 mm h$^{-1}$ were more frequently measured, accounting for over one-fourth of the total count at RSSP.

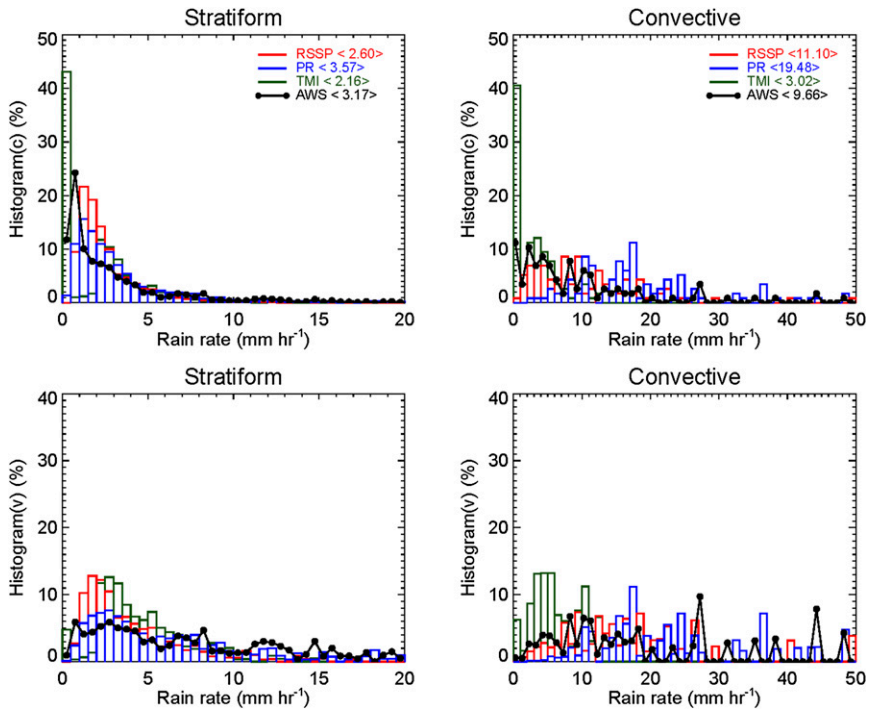


FIG. 11. As in Fig. 10, but for RSSP.

In convective rains, heavy rain rates above 20.0 mm h$^{-1}$ were relatively often measured at discontinuous bins. GR rain rates in stratiform rain showed peaks above 20% of the entire count in the 1.0–2.0 mm h$^{-1}$ bins. The common results in Figs. 10 and 11 are that PR is suitably matched with gauge rates in stratiform rain, and the GR distribution matches up well to gauge rates in convective rain.

The mean rain rates of the original GR, bias-adjusted GR, PR, and gauge, and the mean differences of the two types of GR rain rates between themselves, PR and gauge, at the four GR sites for the stratiform and convective rain types are shown in Tables 3 and 4, respectively. In Table 3, the adjusted GR stratiform rain rates increased about 0.20–0.77 mm h$^{-1}$ over the original GR rates, except at RJNI, where the reflectivity adjustment was negative, thus lowering the GR rain rates in the adjusted values. At the other sites, the means of the bias-adjusted GR rain rates were generally closer to the means of the PR and gauge rain rates. In the case of convective rain (Table 4), the GR rain rates were adjusted away from PR by about −1.3 mm h$^{-1}$ at RJNI, and toward PR by over 3.0 mm h$^{-1}$ at RGSN and RSSP. Excluding at RJNI, the GR mean rain rates after bias adjustment were better aligned with those of PR for both rain types, while the GR adjustment gave mixed results in the convective rain differences with gauge rain rates. The differences of mean rain rates between the ground measurements and satellite observations at RGSN and RSSP were larger compared to the differences at RJNI and RPSN, without the distinction of rain type.

## 4. Summary and conclusions

In the first part of the study, we compared the reflectivities from the attenuation-corrected TRMM PR 2A-25 product to four S-band radars in Jindo, Pusan,

TABLE 3. Mean rain rates (mm h$^{-1}$) and mean rain-rate differences (mm h$^{-1}$) of GR, PR, and gauge on stratiform rain only for 4 years by GR site. Means and mean differences are shown for both original GR (org) and bias-adjusted GR (adj).

| Site ID | GR rain (org) | GR rain (adj) | PR rain | Gauge rain | GR(adj) − GR(org) | PR − GR(org) | PR − GR(adj) | Gauge − GR(org) | Gauge − GR(adj) |
|---|---|---|---|---|---|---|---|---|---|
| RJNI | 3.059 | 2.786 | 3.552 | 3.351 | −0.273 | 0.493 | 0.766 | 0.291 | 0.565 |
| RPSN | 2.298 | 2.494 | 3.258 | 3.140 | 0.195 | 0.959 | 0.764 | 0.842 | 0.646 |
| RGSN | 2.089 | 2.860 | 3.732 | 3.111 | 0.771 | 1.644 | 0.872 | 1.023 | 0.251 |
| RSSP | 1.979 | 2.600 | 3.568 | 3.173 | 0.621 | 1.588 | 0.967 | 1.193 | 0.572 |

TABLE 4. As in Table 3, but for convective rain only.

| Site ID | GR rain (org) | GR rain (adj) | PR rain | Gauge rain | GR(adj) − GR(org) | PR − GR(org) | PR − GR(adj) | Gauge − GR(org) | Gauge − GR(adj) |
|---|---|---|---|---|---|---|---|---|---|
| RJNI | 13.221 | 11.889 | 16.641 | 7.488 | −1.332 | 3.420 | 4.752 | −5.733 | −4.401 |
| RPSN | 9.017 | 9.888 | 15.427 | 8.348 | 0.872 | 6.411 | 5.539 | −0.669 | −1.541 |
| RGSN | 7.252 | 10.354 | 18.634 | 10.608 | 3.102 | 11.382 | 8.280 | 3.356 | 0.254 |
| RSSP | 8.147 | 11.100 | 19.479 | 9.658 | 2.953 | 11.332 | 8.380 | 1.511 | −1.442 |

Gosan, and Seongsan, located on the Korean Peninsula. To assess the offsets in TRMM precipitation radar (PR) and matched ground radars (GRs), a time series of GR data collected from above the bright band (BB) in stratiform rains was compared to matched PR data. The mean reflectivity differences between the PR and GR demonstrated stable and improving variances in the time series analysis for 4 years. For RGSN and RSSP, the negative biases of the GR–PR estimates fluctuated consistently in the −3- to 0-dB$Z$ range. At RPSN, the biases have decreased markedly since 2010. Liao and Meneghini (2009a) showed that the mean difference between the PR and WSR-88D in Melbourne, Florida, from 1998 to 2007 is 0.8 dB$Z$, with positive PR bias relative to WSR-88D. This result is similar in magnitude with that at RJNI. Wang and Wolff (2009) also showed that the PR and GR observations for several years in Houston, Texas; Melbourne, Florida; and Kwajalein Atoll agree to about ±1 dB$Z$ on average, whereas the GR in Darwin, Australia, requires calibration corrections of +1 to −5 dB$Z$. Thus, the reflectivity differences between PR and GRs used in this study are consistent with those observed by previous authors.

Systematic differences in the PR and GR radar reflectivity factor prior to the adjustment for rain cases from August 2006 to August 2010 are as follows. 1) PR reflectivities were found to be about 2–3 dB$Z$ higher than GR at RPSN, RGSN, and RSSP over all altitudes, but PR-measured reflectivities at RJNI were lower than GR by about 1 dB$Z$ on average. 2) Scatterplot analysis categorized by BB height (freezing level) in each rain type showed lower correlations for the stratiform rain above the BB and the convective rain below the BB in general. 3) Significant discrepancies were found in the shapes of the PDFs, in the locations of the maxima, and in the mean biases. The PR peaks shifted significantly toward larger reflectivities by about 3 dB$Z$ with respect to the GR at RGSN and RSSP. At RJNI, the shapes and peaks of PR and unadjusted GR showed similar patterns with small GR–PR biases of about −0.26 dB$Z$ for stratiform rain below the BB, and about 0.25 dB$Z$ for convective rain above the BB. A bias adjustment for each GR was computed as the mean GR − PR reflectivity difference for stratiform rain above the BB. After GR adjustment, PR and GR reflectivities for each rain type and radar site showed a smaller RMSE as well as corrected bias and more fitted distribution in scatterplot and PDF analysis, except at RJNI for stratiform rain below the BB and convective rain at all the levels. At RPSN, the RMSEs decreased 0.25 in stratiform rain and 0.15 in convective rain below BB, which are greater than above and within BB as much as one order. It was more than 1.0 in stratiform rain and 0.94 and 0.82 in convective rain below BB at RGSN and RSSP, respectively. The RMSEs for above BB decreased about 1.02 at RGSN and 0.76 at RSSP regardless of rain type.

Several comparisons of rain rates estimated from the PR, TMI, GR, and rain gauge were performed according to rain type. The results indicated that each measurement has characteristics and sensitivities inherent to rain-rate range and rain type. In stratiform rain, which accounted for about 90% of the total rain occurrence and 70% of the total rain volume around the four radar sites, PR showed relatively good correlations and similar histogram patterns with rain gauge data, although the RMSEs of over 5 times the biases were evident for randomly scattered distributions. The bias-adjusted GR exhibited similar distribution patterns compared with PR, except for peaks in the 1.0–2.5 mm h$^{-1}$ range, while the RMSEs and biases obtained by comparison to gauge data were low relative to PR. Because mean biases applied to GR were obtained from differences with PR reflectivities, retrieval characteristics of the PR sensor were reflected in results of bias-adjusted GR rain rate. As a result, differences between GR and gauge and GR and PR rain rates decreased except for RJNI, where a negative mean bias was applied. TMI rain rates were significantly underestimated compared with the values from rain gauges, and rain volumes in the range of 2.0–3.5 mm h$^{-1}$ were a large percentage of the overall TMI rain-rate volume. This dissimilarity of TMI histograms with the others in the 2.0 mm h$^{-1}$ range was also mentioned by Wolff and Fisher (2008) to be present at Kwajalein Atoll and Melbourne. They concluded that the uniqueness of the retrieved distribution of TMI is due to the effect of coastal areas, where passive microwave estimations are strongly influenced by coastal algorithm uncertainties.

For the convective rain type, TMI significantly underestimated and PR overestimated rain rates as compared to rain gauge data. After GR bias adjustment, distribution patterns of GR rain rates were well matched to gauges in the range of 4.0–20.0 mm $h^{-1}$, and mean biases compared to PR were reduced by about a third. The adjustment process, however, overestimated GR convective rain rates relative to gauge measurements, which was opposite of the stratiform case. Hong (2004) showed thermodynamic mechanisms generated in the Korean Peninsula that were based on the analyses of model simulations for selected heavy rainfall events and summertime climatology over the Korean and the U.S. regions. According to the results, heavy rainfall over the Korean Peninsula is mainly relative to the precipitation physics activated in the presence of supersaturation and strong synoptic-scale forcing rather than convective instability, of which the latter frequently occurs over the U.S. region with large convective available potential energy (CAPE) at the mesoscale. Over the Korean Peninsula in the East Asia region, a strong baroclinicity is more dominant than other regions in the same latitude, especially during summertime. Overestimations of PR rain rates in convective rain, like those shown by Ikai and Nakamura (2003), are possibly connected with low BB height and large path-integrated attenuation (PIA). This is opposite to the results in Melbourne, Florida, measured by Liao and Meneghini (2009a). In Melbourne, the PR-derived rain (version 6) was about 19% less on average than that estimated from the WSR-88D ground radar for convective rain during the period of 1998–2007.

In this study, we focused on understanding the instantaneous measurement characteristics of satellite and ground-based radar in the Korean Peninsula using relative bias between rainfall estimations of each instrument around East Asia. To correspond with our goal, the GV system has been optimized on the Korean Peninsula, and the results have proved that the software functioned stably. The original GR, bias-corrected GR, and PR rain rate were evaluated by comparing with the gauge rain rate in section 3b. The results and previous researches suggested that relative bias adjustments should be taken into account in evaluating satellite retrievals around East Asia. We used a simple method to test bias-correction effects in rain rate through adding the mean difference of measured reflectivities between PR and GR to the original GR before applying the $Z$–$R$ relation. If regular differences are also found in the dual-frequency precipitation radar (DPR) and GR, which remain independent of the satellite estimates using the same ground validation system when the GPM mission is started, then it means the validation system is worth utilizing and improves sustainably. In the next stage, the bias correction and recalibration using the advanced statistical method would be considered to the GV system, but more work remains to be done to improve the matchup to gauge measurements in this region, including representativeness of the instantaneous gauge rain rates over a coarser grid scale (Zawadzki 1975; Kitchen and Blackall 1992; Habib et al. 2009). The GR estimates should be kept independent of the satellite estimates but be adjusted to the gauges when they are used for validation of the satellite estimates. As we can see in Fig. 1, and that the horizontal domains of RJNI and two other radars on the southern island overlap quite a large area even at 100-km range, a couple of GR pixels in two or three GR domains could be matched to one PR pixel. In this study, views of different GR of the identical PR view were included in the statistical analysis of each GR in order to examine the average tendency of validation results at each GR site. It can be considered that the closest GR pixel with a PR view is selected or the pixels from two or three GRs on the overlap are averaged when satellite reflectivities are validated.

Future work will also cover the physical analysis of PR, TMI, and GR, reflecting the precipitation microphysics around East Asia as well as a direct statistical comparison. Hence, it is necessary to utilize statistics from various independent estimations for validation.

*Acknowledgments.* This study was supported by the Research for the Meteorological and Earthquake Observation Technology and Its Application of the National Institute of Meteorological Research, Korea Meteorological Administration (KMA), South Korea. The authors thank the NASA Goddard Space Flight Center (GSFC) for providing data processing software for the GPM Ground Validation System (GVS) and TRMM products.

## REFERENCES

Anagnostou, E., C. Morales, and T. Dinku, 2001: The use of TRMM precipitation radar observations in determining ground radar calibration biases. *J. Atmos. Oceanic Technol.,* **18,** 616–628, doi:10.1175/1520-0426(2001)018<0616:TUOTPR>2.0.CO;2.

Bolen, S. M., and V. Chandrasekar, 2000: Quantitative cross validation of space-based and ground-based radar observations. *J. Appl. Meteor.,* **39,** 2071–2079, doi:10.1175/1520-0450(2001)040<2071:QCVOSB>2.0.CO;2.

——, and ——, 2003: Methodology for aligning and comparing spaceborne radar and ground-based radar observations. *J. Atmos. Oceanic Technol.,* **20,** 647–659, doi:10.1175/1520-0426(2003)20<647:MFAACS>2.0.CO;2.

Durden, S. L., Z. S. Haddad, A. Kitiyakara, and F. K. Li, 1998: Effects of nonuniform beam filling on rainfall retrieval for the TRMM precipitation radar. *J. Atmos. Oceanic Technol.,* **15,** 635–646, doi:10.1175/1520-0426(1998)015<0635:EONBFO>2.0.CO;2.

Ferraro, R. R., 1997: Special Sensor Microwave Imager derived global rainfall estimates for climatological applications. *J. Geophys. Res.,* **102,** 16 715–16 735, doi:10.1029/97JD01210.

Gabella, M., J. Joss, S. Michaelides, and G. Perona, 2006: Range adjustment for ground-based radar, derived with the spaceborne TRMM precipitation radar. *IEEE Trans. Geosci. Remote Sens.,* **44,** 126–133, doi:10.1109/TGRS.2005.858436.

Ha, E., and G. R. North, 1999: Error analysis for some ground validation designs for satellite observations of precipitation. *J. Atmos. Oceanic Technol.,* **16,** 1949–1957, doi:10.1175/1520-0426(1999)016<1949:EAFSGV>2.0.CO;2.

Habib, E., W. Krajewski, and A. Kruger, 2001: Sampling errors of tipping bucket rain gauge measurements. *J. Hydrol. Eng.,* **6,** 159–166, doi:10.1061/(ASCE)1084-0699(2001)6:2(159).

——, B. Larson, and J. Graschel, 2009: Validation of NEXRAD multisensor precipitation estimates using an experimental dense rain gauge network in south Louisiana. *J. Hydrol.,* **373,** 463–478, doi:10.1016/j.jhydrol.2009.05.010.

Hitschfeld, W., and J. Bordan, 1954: Errors inherent in the radar measurements of rainfall at attenuating wavelengths. *J. Meteor.,* **11,** 58–67, doi:10.1175/1520-0469(1954)011<0058:EIITRM>2.0.CO;2.

Hong, S.-Y., 2004: Comparison of heavy rainfall mechanisms in Korea and the central US. *J. Meteor. Soc. Japan,* **82,** 1469–1479, doi:10.2151/jmsj.2004.1469.

Hou, A. Y., G. Skofronick-Jackson, C. D. Kummerow, and J. M. Shepherd, 2008: Global precipitation measurement. *Precipitation: Advances in Measurement, Estimation and Prediction,* S. C. Michaelides, Ed., Springer, 131–169.

Humphrey, M. D., J. D. Istok, J. Y. Lee, J. A. Hevesi, and A. L. Flint, 1997: A new method for automated dynamic calibration of tipping-bucket rain gauges. *J. Atmos. Oceanic Technol.,* **14,** 1513–1519, doi:10.1175/1520-0426(1997)014<1513:ANMFAD>2.0.CO;2.

Iguchi, T., T. Kozu, R. Meneghini, J. Awaka, and K. Okamoto, 2000: Rain-profiling algorithm for the TRMM precipitation radar. *J. Appl. Meteor.,* **39,** 2038–2052, doi:10.1175/1520-0450(2001)040<2038:RPAFTT>2.0.CO;2.

Ikai, J., and K. Nakamura, 2003: Comparison of rain rates over the ocean derived from TRMM Microwave Imager and precipitation radar. *J. Atmos. Oceanic Technol.,* **20,** 1709–1726, doi:10.1175/1520-0426(2003)020<1709:CORROT>2.0.CO;2.

Kitchen, M., and R. M. Blackall, 1992: Representativeness errors in comparisons between radar and gauge measurements of rainfall. *J. Hydrol.,* **134,** 13–33, doi:10.1016/0022-1694(92)90026-R.

Kozu, T., and T. Iguchi, 1999: Nonuniform beamfilling correction for spaceborne radar rainfall measurement: Implications from TOGA COARE radar data analysis. *J. Atmos. Oceanic Technol.,* **16,** 1722–1735, doi:10.1175/1520-0426(1999)016<1722:NBCFSR>2.0.CO;2.

——, and Coauthors, 2001: Development of precipitation radar onboard the Tropical Rainfall Measuring Mission (TRMM) satellite. *IEEE Trans. Geosci. Remote Sens.,* **39,** 102–116, doi:10.1109/36.898669.

Kummerow, C., W. S. Olson, and L. Giglio, 1996: A simplified scheme for obtaining precipitation and vertical hydrometeor profiles from passive microwave sensors. *IEEE Trans. Geosci. Remote Sens.,* **34,** 1213–1232, doi:10.1109/36.536538.

——, W. Barnes, T. Kozu, J. Shiue, and J. Simpson, 1998: The Tropical Rainfall Measuring Mission (TRMM) sensor package. *J. Atmos. Oceanic Technol.,* **15,** 809–817, doi:10.1175/1520-0426(1998)015<0809:TTRMMT>2.0.CO;2.

——, and Coauthors, 2001: The evolution of the Goddard profiling algorithm (GPROF) for rainfall estimation from passive microwave sensors. *J. Appl. Meteor.,* **40,** 1801–1820, doi:10.1175/1520-0450(2001)040<1801:TEOTGP>2.0.CO;2.

Liao, L., and R. Meneghini, 2009a: Validation of TRMM precipitation radar through comparison of its multiyear measurements with ground-based radar. *J. Appl. Meteor. Climatol.,* **48,** 804–817, doi:10.1175/2008JAMC1974.1.

——, and ——, 2009b: Changes in the TRMM version-5 and version-6 precipitation radar products due to orbit boost. *J. Meteor. Soc. Japan,* **87A,** 93–107, doi:10.2151/jmsj.87A.93.

——, ——, and T. Iguichi, 2001: Comparisons of rain rate and reflectivity factor derived from the TRMM precipitation radar and the WSR-88D over the Melbourne, Florida, site. *J. Atmos. Oceanic Technol.,* **18,** 1959–1974, doi:10.1175/1520-0426(2001)018<1959:CORRAR>2.0.CO;2.

McCollum, J. R., and R. R. Ferraro, 2003: Next generation of NOAA/NESDIS TMI, SSM/I, and AMSR-E microwave land rainfall algorithms. *J. Geophys. Res.,* **108,** 8382, doi:10.1029/2001JD001512.

——, and ——, 2005: Microwave rainfall estimation over coasts. *J. Atmos. Oceanic Technol.,* **22,** 497–512, doi:10.1175/JTECH1732.1.

Meneghini, R., T. Iguchi, T. Kozu, L. Liao, K. Okamoto, J. Jones, and J. Kwiatkowski, 2000: Use of the surface reference technique for path attenuation estimates from the TRMM precipitation radar. *J. Appl. Meteor.,* **39,** 2053–2070, doi:10.1175/1520-0450(2001)040<2053:UOTSRT>2.0.CO;2.

Morris, K. R., and M. R. Schwaller, 2011: Sensitivity of spaceborne and ground radar comparison results to data analysis methods and constraints. *35th Conf. on Radar Meteorology,* Pittsburgh, PA, Amer. Meteor Soc, 68. [Available online at https://ams.confex.com/ams/35Radar/webprogram/Paper191729.html.]

Negri, A., T. Bell, and L. Xu, 2002: Sampling of the diurnal cycle of precipitation using TRMM. *J. Atmos. Oceanic Technol.,* **19,** 1333–1344, doi:10.1175/1520-0426(2002)019<1333:SOTDCO>2.0.CO;2.

Nespor, V., and B. Sevruk, 1999: Estimation of wind-induced error of rainfall gauge measurements using a numerical simulation. *J. Atmos. Oceanic Technol.,* **16,** 450–464, doi:10.1175/1520-0426(1999)016<0450:EOWIEO>2.0.CO;2.

Olson, W. S., C. D. Kummerow, Y. Hong, and W.-K. Tao, 1999: Atmospheric latent heating distributions in the tropics derived from satellite passive microwave radiometer measurements. *J. Appl. Meteor.,* **38,** 633–664, doi:10.1175/1520-0450(1999)038<0633:ALHDIT>2.0.CO;2.

——, and Coauthors, 2006: Precipitation and latent heating distributions from satellite passive microwave radiometry. Part I: Improved method and uncertainty estimates. *J. Appl. Meteor. Climatol.,* **45,** 702–720, doi:10.1175/JAM2369.1.

Rosenfeld, D., D. Atlas, D. B. Wolff, and E. Amitai, 1992: Beamwidth effects on *Z–R* relations and area-integrated rainfall. *J. Appl. Meteor.,* **31,** 454–464, doi:10.1175/1520-0450(1992)031<0454:BEOZRR>2.0.CO;2.

Schumacher, C., and R. A. Houze Jr., 2000: Comparison of radar data from the TRMM satellite and Kwajalein oceanic validation site. *J. Appl. Meteor.,* **39,** 2151–2164, doi:10.1175/1520-0450(2001)040<2151:CORDFT>2.0.CO;2.

Schwaller, M. R., and K. R. Morris, 2011: A ground validation network for the Global Precipitation Measurement mission. *J. Atmos. Oceanic Technol.,* **28,** 301–319, doi:10.1175/2010JTECHA1403.1.

Seo, E. K., B. J. Sohn, and G. Liu, 2007: How TRMM precipitation radar and microwave imager retrieved rain rates differ. *Geophys. Res. Lett.,* **34,** L24803, doi:10.1029/2007GL032331.

Simpson, J., R. F. Adler, and G. R. North, 1988: A proposed Tropical Rainfall Measuring Mission (TRMM) satellite. *Bull. Amer. Meteor. Soc.,* **69,** 278–295, doi:10.1175/1520-0477(1988)069<0278:APTRMM>2.0.CO;2.

Sohn, B. J., H.-J. Han, E.-K. Seo, 2010: Validation of satellite-based high-resolution rainfall products over the Korean Peninsula using data from a dense rain gauge network. *J. Appl. Meteor. Climatol.,* **49,** 701–714, doi:10.1175/2009JAMC2266.1.

Spencer, R., W. H. Goodman, and R. E. Hood, 1989: Precipitation retrieval over land and ocean with the SSM/I: Identification and characteristics of the scattering signal. *J. Atmos. Oceanic Technol.,* **6,** 254–273, doi:10.1175/1520-0426(1989)006<0254:PROLAO>2.0.CO;2.

Wang, J., and D. B. Wolff, 2009: Comparisons of reflectivities from the TRMM precipitation radar and ground-based radars. *J. Atmos. Oceanic Technol.,* **26,** 857–875, doi:10.1175/2008JTECHA1175.1.

——, B. L. Fisher, and D. B. Wolff, 2008: Estimating rain rates from tipping-bucket rain gauge measurements. *J. Atmos. Oceanic Technol.,* **25,** 43–56, doi:10.1175/2007JTECHA895.1.

Wolff, D. B., and B. L. Fisher, 2008: Comparisons of instantaneous TRMM ground validation and satellite rain-rate estimates at different spatial scales. *J. Appl. Meteor. Climatol.,* **47,** 2215–2237, doi:10.1175/2008JAMC1875.1.

——, D. A. Marks, E. Amitai, D. S. Silberstein, B. L. Fisher, A. Tokay, J. Wang, and J. L. Pippitt, 2005: Ground validation for the Tropical Rainfall Measuring Mission (TRMM). *J. Atmos. Oceanic Technol.,* **22,** 365–380, doi:10.1175/JTECH1700.1.

Zagrodnik, J. P., and H. Jiang, 2013: Investigation of PR and TMI version 6 and version 7 rainfall algorithms in landfalling tropical cyclones relative to the NEXRAD stage-IV multisensor precipitation estimate dataset. *J. Appl. Meteor. Climatol.,* **52,** 2809–2827, doi:10.1175/JAMC-D-12-0274.1.

Zawadzki, I., 1975: On radar-raingage comparison. *J. Appl. Meteor.,* **14,** 1430–1436, doi:10.1175/1520-0450(1975)014<1430:ORRC>2.0.CO;2.